Optics & Laser Technology 177 (2024) 111121

Contents lists available at ScienceDirect

Optics and Laser Technology

journal homepage: www.elsevier.com/locate/optlastec

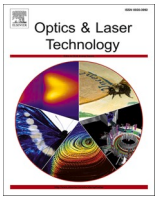

Full length article

Quantitative phase imaging by automated Cepstrum-based interferometric microscopy (CIM)

Ricardo Rubio-Oliver [a], Vicente Micó [a,*], Zeev Zalevsky [b], Javier García [a], Jose Angel Picazo-Bueno [a,c]

[a] Departamento de Óptica y de Optometría y Ciencias de la Visión. Facultad de Física. Universidad de Valencia. C/ Doctor Moliner 50, 46100 Burjassot, Spain
[b] School of Enginering, Bar-Ilan University, Ramat-Gan 52900, Israel
[c] Biomedical Technology Center, University of Muenster, Mendelstr. 17, D-48149 Muenster, Germany

ARTICLE INFO

Keywords:
Quantitative phase imaging
Digital holographic microscopy
Phase retrieval
Cepstrum transform
Unknown reference beam
Interference microscopy

ABSTRACT

Digital holographic microscopy (DHM) is a very popular interferometric technique for quantitative phase imaging (QPI). In DHM, an interferometer is combined with a microscope to create interference between an imaging beam containing information about the analysed sample and a clear reference beam carrying no sample information. To exploit the capability of reference beam in terms of useful sample information, we have recently proposed Cepstrum-based Interferometric Microscopy (CIM) [Opt. Las. Tech. 174, 110,626 (2024)] as a novel methodology involving the interference of two imaging beams carrying different sample information and to accurately retrieve quantitative phase data of both beams. In the earlier implementation, proof-of-concept of CIM was demonstrated for a Michelson-based layout requiring manual adjustments during the CIM methodology and validated only for low numerical aperture (NA) microscope lenses. In this contribution, we present a new CIM arrangement that provides precise QPI with medium NA microscope lenses and avoids manual intervention of the user during the hologram recording. This new approach incorporates a compact quasi-common-path Mach-Zehnder configuration at the output port of an infinity corrected microscope system to interfere two imaging beams containing information from different regions of the sample. By sequentially recording three off-axis holograms and applying the Spatial-Shifting Cepstrum (SSC) algorithm, decoupled QPI of both complex fields are retrieved, doubling the accessible field of view (FOV). The effectiveness of the approach is experimentally validated using two medium NA microscope lenses with distinct features (20x/0.42NA and 50x/0.55NA). The approach is first validated with calibrated phase objects, and then assessed for imaging of various biological samples.

1. Introduction

Quantitative phase imaging (QPI) is a valuable label-free and wide-field optical microscopy method with outstanding possibilities for biomedical applications [1,2]. QPI exploits the intrinsic phase shift of light passing through transparent samples, such as cells and tissues, to provide high endogenous contrast imaging and to quantify different biophysical parameters such as, for example, refractive index (RI), topography or dry mass [3,4]. Hence, QPI can provide valuable information about cell size, morphology, behavior, cellular viscoelasticity, drug efficacy, biomass accumulation or transport mechanics, which are supporting studies of development, physiology, neural activity, cancer and additional physiological processes and disease [5]. QPI can be achieved by diverse techniques based on different interferometric and non-interferometric basic principles [6–13], being interferometric techniques, in particular digital holographic microscopy (DHM), maybe the most widely used for QPI [11,14–16].

DHM merges high-quality imaging, interferometric accuracy and computational processing and analysis, provides extended depth of field, enables numerical refocusing, and allows whole-object wavefront recovery with nanometer sensitivity [11,17–19]. In addition, DHM enables QPI using a wide-field, real-time, non-invasive, non-contact, and static operating principle. In DHM, a clean external reference beam with known complex amplitude distribution interferes with the original object beam in the recording plane forming a hologram, from which QPI is achieved by numerical reconstruction [15].

* Corresponding author.
E-mail address: vicente.mico@uv.es (V. Micó).

https://doi.org/10.1016/j.optlastec.2024.111121
Received 5 February 2024; Received in revised form 7 April 2024; Accepted 30 April 2024

Various classical interferometric configurations, including Mach-Zehnder [20,21], Michelson [22], Linnik [23], Mirau [24], Twyman-Green [25] and common-path arrangements [26] are commonly used in DHM, with Mach-Zehnder being the most widely used architecture in practice. Historically, the requirement of a clean reference beam for interferometric recording in DHM-based QPI has been mandatory, regardless of the specific interferometric setup utilized. In essence, the success of DHM imaging relies on prior knowledge of the complex amplitude distribution of one of the interferometric beams, the reference one. With this prior knowledge, one can subsequently retrieve the complex amplitude information of the other beam involved, the object one. Until now, the necessity of a reference beam with a known complex amplitude distribution has been a universal requirement in all holographic approaches.

Recently, we have proposed a DHM technique that achieves QPI from both unknown/arbitrary interferometric beams [27]. The technique is named Cepstrum-based Interferometric Microscopy (CIM) and supposes a huge step forward not only in DHM but also in holography and interferometry, to remove the barrier of using clean/known reference beams for interferometric recording and QPI reconstruction [27]. CIM provides accurate QPI of all arbitrary interferometric beams involved in the recording process. In our previous approach, CIM was able to recover QPI of the three complex fields involved in the recording process, thus also tripling the field of view (FOV) [27]. In [27], proof-of-concept of CIM technique was reported using a Michelson-based layout and a low numerical aperture (NA) and magnification microscope lens (7.5x/0.21NA).

In this contribution, we present a new CIM approach based on a Mach-Zehnder arrangement and medium NA/magnification microscope lenses. The approach implements a quasi-common-path interferometric configuration at the output port of a microscopy system based on a compact Mach-Zehnder interferometer, where both interferometric beams carry information of different regions of the sample. The methodology records three off-axis holograms, where one of the interferometric beams is shifted in both transversal directions (x and y) a small amount (1-pixel of the digital sensor) around a starting position. Afterwards, the approach implements the Spatial-Shifting Cepstrum (SSC) algorithm introduced in our previous paper [27] and performs a decoupling procedure to provide separate QPI of both interferometric beams. The proposed approach is a step forward in the potential of CIM to be applied to real biomedical applications, which commonly make use of optical microscopes with medium NA and magnification microscope lenses, such as in cell biology, microbiology or histology. In addition, the new arrangement increases flexibility and versatility, avoids manual adjustment of the optical components between acquisitions because automatizes completely the recording process. As result, the new automated CIM approach significantly increases the acquisition speed and robustness of CIM technique while ensures repeatability of the results. This opens new possibilities to CIM for, for instance, pseudo real-time or time-lapse biological applications. The manuscript is organized as follows. Section 2 describes the experimental layout and methodology for interferometric recording and QPI reconstruction and FOV decoupling. Section 3 includes the experimental validations for different samples (phase resolution test target and biological fixed cells and tissue sections). Finally, Sections 4 and 5 discusses and concludes the manuscript, respectively.

2. System analysis and methodology

2.1. Automated CIM layout description

Fig. 1 includes an optical scheme [Fig. 1(a)] and a picture [Fig. 1(b)] of the experimental setup utilized for validation of automated CIM. The layout was composed of a common-path Mach-Zehnder interferometer together with an infinity corrected microscope arranged on an optical table. For illuminating the sample with coherent light, we utilized a laser

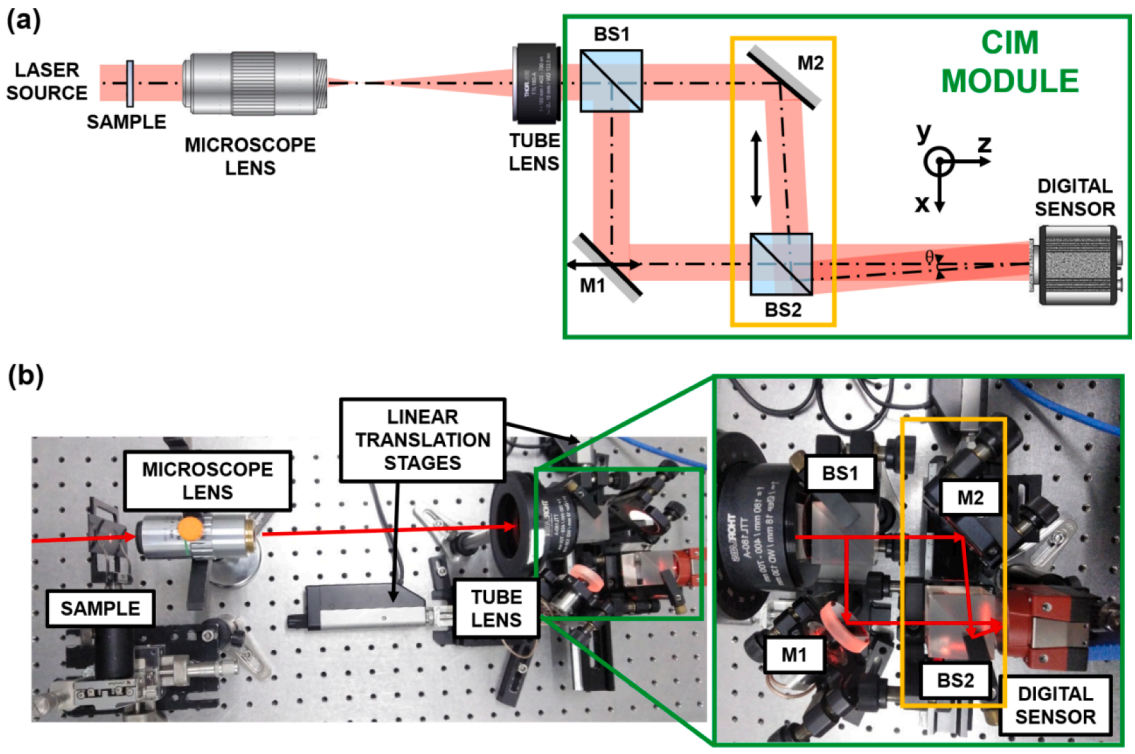

Fig. 1. Experimental system for automated CIM implementation. (a) Schematic representation of the optical scheme including the main components of the layout and highlighting the CIM module. (b) Picture of the complete system and enlarged image of the CIM module, marked with a green rectangle. Orange rectangles included in (a) and (b) highlight the components with a joint movement. (For interpretation of the references to color in this figure legend, the reader is referred to the web version of this article.)

source (He-Ne, λ = 632.8 nm, optical power 35 mW). The lab-made microscopy arrangement consisted of a microscope objective (20x / 0.42NA and 50x / 0.55NA, infinity corrected, LD, Mitutoyo, Japan) and a tube lens (TTL180-A, 180 mm focal length, Thorlabs, US). Behind the tube lens, we assembled a compact Mach-Zehnder interferometer for automated CIM implementation, having dimension of 12 x 12 cm (excluding motorized stages).

The CIM module [marked with green rectangles in Fig. 1(a) and (b)] was composed of two beam splitter cubes (BS013, 50:50 R-T, 25.4 mm side, non-polarizing, Thorlabs, US) and two mirrors (PF10-03-G01, 25.4 mm diameter, round protected aluminum, Thorlabs, US). For automated CIM implementation, precise vertical and horizontal movements of interferometric beams were produced by two linear translation stages (8500G-HL, Newport, US) controlled by high precision actuators (SP300 Motion Controller/Driver, Newport, US). The mirror M1 was moved along z-axis direction by means of a linear translation stage to provide the horizontal shift along the x-axis direction. Furthermore, another linear translation stage controlled together the mirror M2 and the recombining beam splitter cube BS2 along the x-axis direction to induce the vertical movement of the FOV in the y-axis direction. This vertical shift provided by the combination of M2-BS2 components was due to M2 was tilted in the vertical y-axis direction to induce the off-axis holographic configuration in such a vertical direction. This vertical off-axis holographic configuration can be better identified in the Fourier transforms of the recorded holograms included in Fig. 2(c1) and (c2). This mechanical configuration avoids the manual adjustment of one of the mirrors and enables the automatization of the recording process, which increases the recording speed and ensures repeatability in the recording process, unlike the previously reported arrangement [27]. Digital recording of the three distinct holograms was sequentially done with a complementary metal–oxide–semiconductor (CMOS) sensor (Alvium 1800U-811 m, monochrome, USB3.0, pixel size 2.74 µm, resolution 2848 x 2848 pixel, global shutter, frame rate 51 fps, Allied Vision, Germany). Subsequent digital image processing was carried out in a laptop (XPS15 9550, Dell, US) employing a numerical computing platform (MATLAB 2021b).

2.2. CIM holographic recording

In the new automated CIM implementation we are presenting, a total of three off-axis holograms are needed. These three holograms are sequentially recorded starting from two independent complex fields. After an initial off-axis recording, one of those interferometric images is first vertically and after horizontally shifted by one pixel providing the two additional recordings. In our case, the shift was produced by a precision motor actuator with high enough displacement accuracy running at a constant speed. As in previous CIM implementation, 40 frames integrating a displacement of one pixel were recorded after

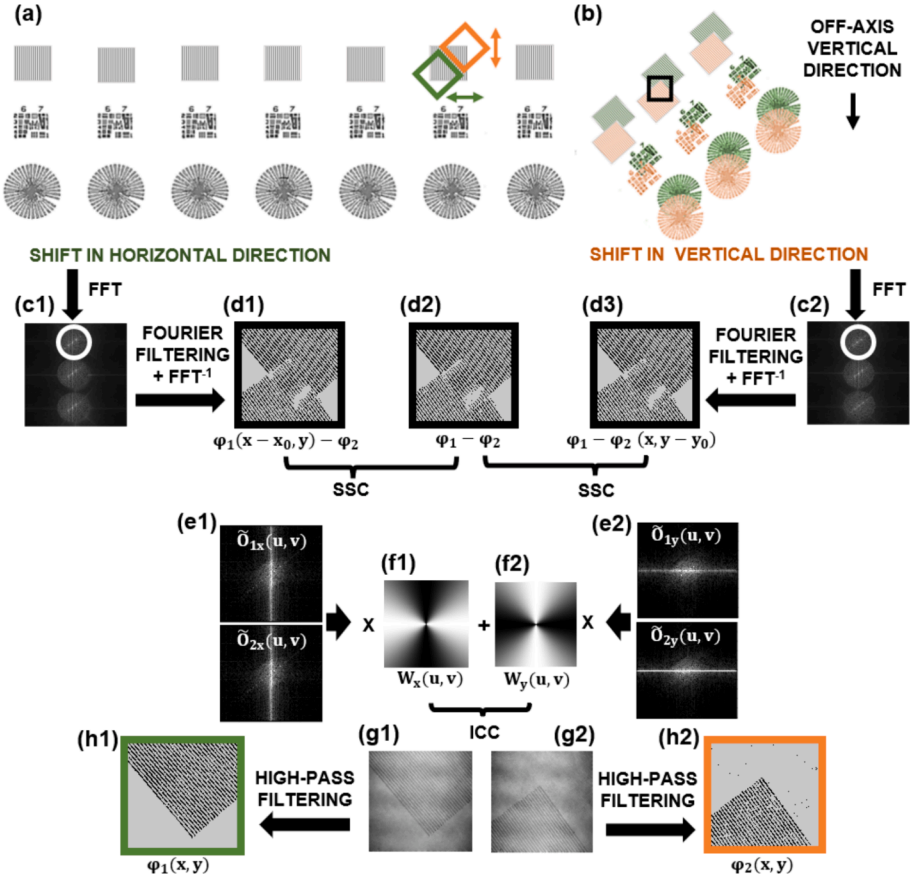

Fig. 2. Flow chart of the recovery process of the proposed automated CIM approach. (a) Scheme of the calibrated phase object involved in the experimental validation indicating the 2 FOVs involved in the process (green and orange squares, with colored arrows showing the shift). (b) Arrangement of the FOVs in the phase target after off-axis holographic configuration in vertical direction. (c1) and (c2) Fourier transforms of the holograms recorded considering the horizontal and vertical shifts, respectively. (d1)-(d3) QPIs recovered from the three distinct holograms after Fourier filtering [white circles included in (c1) and (c2)] and inverse Fourier transform. (e1) and (e2) Fourier transforms recovered after application of the SSC algorithm considering the image combinations (d1)-(d2) and (d2)-(d3), respectively. (f1) and (f2) bow-tie masks applied to Fourier transforms of (e1) and (e2) to remove spatial frequency singularities in vertical and horizontal directions, respectively. (g1) and (g2) phase reconstructions from the combination (e1)-(f1) and (e2)-(f2) after ICC, respectively. (h1) and (h2) Final QPIs recovered after high-pass filtering process to (g1) and (g2), respectively. Note that in images (d1)-(d3) and (h1)-(h2) contrast was increased for shake of clarity in the visualization, proper phase images are depicted in Fig. 3. (For interpretation of the references to color in this figure legend, the reader is referred to the web version of this article.)

reaching the steady velocity of the motor, thus having an estimated determination confidence of 1/40 of pixel [27]. This process was performed in both vertical and horizontal directions and the accuracy and repeatability were determined using an amplitude object (USAF resolution target, Newport, US) and a subpixel cross-correlation image registration algorithm in an initial calibration process.

2.3. CIM image reconstruction: SSC algorithm

Once recorded the three off-axis holograms required for CIM application, we implemented the following numerical reconstruction for QPI of the two interferometric beams. Fig. 2 depicts a flow chart of the reconstruction procedure, showing an example with a calibrated phase object. Fig. 2(a) shows a representation of the phase structures of the calibrated target, including green and orange squares to highlight the FOVs considered for reconstruction. In this case, the green and orange squares refer to FOV_1 and FOV_2, respectively. Furthermore, the color-coded arrows included in Fig. 2(a) indicate the shift direction of each FOV. In addition, Fig. 2(b) includes a representation of the arrangement of the FOVs after vertical off-axis holographic configuration, where the black square marks the area recorded by the digital sensor. First, considering the Fourier transforms of the recorded off-axis holograms [see two examples in Fig. 2(c1) and (c2)], we performed conventional Fourier filtering recovery process [28] to each hologram for the obtention of one of the cross-correlation terms of the hologram, which can be denoted as

$$\widehat{U}(u,v) = \widehat{O}_1(u,v) \otimes \widehat{O}_2^{*}(u,v) \tag{1}$$

where $\otimes$ denotes convolution and $\widehat{O}_1(u,v)$ and $\widehat{O}_2^{*}(u,v)$ are the Fourier transforms of the unknown complex amplitudes $O_1(x,y)$ and $O_2(x,y)$ of the interferometric beams including FOV_1 and FOV_2, respectively. In addition, u and v are the spectral coordinates, and x and y are the spatial coordinates. Representations of the three phase images obtained after Fourier filtering are included in Fig. 2(d1), (d2) and (d3). In Eq. (1), we can see that the cross-correlation term presents the information coming from the different beams coupled, so that we must decouple this mixed information to properly retrieve the complex images. In addition, the convolution of Eq. (1) of one complex fields $\widehat{O}_1(u,v)$ with the complex conjugate of the other complex field $\widehat{O}_2^{*}(u,v)$ makes that the phase distributions coming from the different beams have opposite sign, which can derive in phase cancellation in the image regions where object structures, with the same phase values, overlap each other. This mixture of information can be also seen in the phase images of Fig. 2(d1)–(d3), where the spatial overlapping of phase structures coming from the different FOVs induce phase cancellation in some regions of the images.

Decoupling of the images is carried out with the Spatial-Shifting-Cepstrum (SSC) algorithm [27]. As demonstrated in Ref. [27], the amplitude $|O_{1,x}(x,y)|$ and phase $\varphi_{1,x}(x,y)$ distributions of the complex amplitude $O_{1,x}(x,y)$ recovered when considering the shift x_0 in the horizontal direction are given by

$$|O_{1,x}(x,y)| = \exp\left(F^{-1}\left\{\frac{F\{\log(|U(x,y)|) - \log(|U_x(x,y)|)\}}{1 - e^{-i2\pi u x_0}}\right\}\right) \tag{6}$$

$$\varphi_{1,x}(x,y) = \mathscr{F}^{-1}\left\{\frac{\mathscr{F}\{\varphi_U(x,y) - \varphi_{U_x}(x,y)\}}{1 - e^{-i2\pi u x_0}}\right\} \tag{7}$$

where $\varphi_{1,x}(x,y)$, $\varphi_U(x,y)$ and $\varphi_{U_x}(x,y)$ are the phases of the complex fields $O_{1,x}(x,y)$, $U(x,y)$ and $U_x(x,y)$, respectively, being $U_x(x,y)$ the complex amplitude of the cross-correlation term after shifting 1-pixel $O_{1,x}(x,y)$ in x direction. Afterwards, $O_{2,x}(x,y)$ is recovered from $O_{1,x}(x,y)$ as

$$O_{2,x}(x,y) = log^{-1}\left[\mathscr{F}^{-1}\left\{\widetilde{U}(u,v) - \widetilde{O}_{1,x}(u,v)\right\}\right] \tag{8}$$

being $\widetilde{U}(u,v)$ and $\widetilde{O}_{1,x}(u,v)$ the complex Cepstra of $U(x,y)$ and $O_{1,x}(x,y)$, defined as described in [27]. Similar numerical procedure is performed considering the shift y_0 in the vertical direction and the complex fields $O_{1,y}(x,y)$, $O_{2,y}(x,y)$ and $O_{2,y}(x,y-y_0)$. In this case, the shift is performed in the complex amplitude $O_{2,y}(x,y)$, so that we first recover $O_{2,y}(x,y)$ considering Eqs. (6) and (7), and then $O_{1,y}(x,y)$ is achieved taking into account Eq. (8). In Fig. 2(e1) and (e2), we can see the complex Cepstra recovered for $O_{1,x}(x,y)$ and $O_{2,x}(x,y)$, and for $O_{1,y}(x,y)$ and $O_{2,y}(x,y)$, respectively.

As we can see in Fig. 2(e1) and (e2), the complex Cepstra present a centered line of indeterminate values along vertical and horizontal directions, respectively, which is called the zero-ambiguity problem [27]. These lines with indeterminate values can be reduced only to the central DC spatial frequency at the Fourier domain ($u = 0, v = 0$) by averaging both complex reconstructions coming from both horizontal and vertical shifts. On one hand, $O_{1,x}(x,y)$ is combined with $O_{1,y}(x,y)$ and, on the other hand, $O_{2,x}(x,y)$ is merged with $O_{2,y}(x,y)$. To avoid indeterminate values and to ensure smooth transition between determinate-indeterminate values, we apply a bow-tie masking procedure by considering the complex Cepstra showed in Fig. 2(e1) and (e2) and the masks $W_x(u,v)$ and $W_y(u,v)$ depicted in Fig. 2(f1) and (f2), respectively, which are mathematically represented as

$$W_x(u,v) = cos^2\left[\arctan\left(\frac{v}{u}\right)\right] \tag{9}$$

$$W_y(u,v) = sin^2\left[\arctan\left(\frac{v}{u}\right)\right] \tag{10}$$

Then, complex amplitudes of both interferometric beams $O_1(x,y)$ and $O_2(x,y)$ are obtained after inverse complex Cepstrum (ICC) application [27]. Afterwards, QPIs of both beams are achieved by application of a numerical phase unwrapping algorithm [29]. The resulting phase images after ICC and phase unwrapping implementation are included in Fig. 2(g1) and (g2) for the case of the FOV_1 and FOV_2, respectively.

Since in practice, indeterminate values are also expanded to u and v values in the close neighbourhood, background inhomogeneities appear in the recovered complex images [see Fig. 2(g1) and (g2)], which are not critical to retrieve the object information. Removal of background noise is overcome by applying a high-pass filtering process to the recovered complex fields, thus achieving the final QPIs [$\varphi_1(x,y)$ and $\varphi_2(x,y)$] corresponding to $O_1(x,y)$ and $O_2(x,y)$. Such QPIs are included in Fig. 2 (h1) and (h2) for the case of FOV_1 and FOV_2. With this procedure, CIM decouples the information coming from both interferometric beams, thus also doubling the analysed FOV in comparison with conventional DHM techniques.

3. Experimental validation

The automated CIM approach was experimentally validated involving diverse samples and considering several microscope lenses having different NAs and magnifications (20x/0.42NA and 50x/0.55NA). First, we validated the decoupling capability and the QPI performance of the CIM approach with calibrated phase objects. Afterwards, the proposed approach was evaluated for imaging of diverse biological samples containing fixed cells and tissue sections.

3.1. Experimental validation with calibrated phase objects

First validation for successful FOV decoupling and accurate QPI involves a calibrated phase object. In particular, we employed a commercially available quantitative phase target (QPT^{TM}) (https://benchmarktech.com/quantitativephasemicroscop/, Benchmark

Technologies, MA, USA), which contained several structures with seven distinct feature thicknesses from 50 nm to 350 nm with nominal increments of 50 nm. According to the manufacturer, the phase structures were raised on a Corning Eagle XG glass substrate, having a RI value of ~ 1.51 at $\lambda = 632.8$ nm. Estimated thickness values of the phase target features were measured by the manufacturer with atomic force microscopy (AFM).

In a first experiment, a square grid (250 x 250 μm), typically used by the manufacturer for AFM measurements, having a thickness of 300 nm and a spatial period of 2 μm, was imaged with a 20x/0.42NA microscope lens. Fig. 3 shows the results obtained for the FOVs indicated in Fig. 2 from the decoupling procedure performed with the SSC algorithm. Fig. 3 (a) includes the QPI recovered after application of the Fourier filtering method to one of the three recorded off-axis holograms, where the overlapping between the phase structures within the different FOVs is evident. Indeed, due to the opposite sign of the phase presented in the interferometric beams, such overlapping of the structures induced phase cancellation in the region of interest (ROI) marked with a red rectangle, as we can better identify in the enlarged image of such ROI [see Fig. 3 (a)]. In addition, Fig. 3(b) and (c) present QPI reconstructions of FOV_1 and FOV_2 after implementation of the SSC decoupling algorithm, respectively. In the QPIs, we can notice that both FOVs are successfully decoupled each other by SSC method. Furthermore, the application of the SSC algorithm removed the phase cancellation effect, as we can better identify in the enlarged images of the ROIs within the green and blue rectangles included in Fig. 3(b) and (c), respectively. In fact, QPI reconstructions after SSC implementation exhibit spatial distributions expected for such a kind of periodic structure.

To validate the technique from a quantitative point of view, we compared the experimental results provided by the proposed automated CIM approach with those provided by a conventional off-axis DHM layout (a Mach-Zehnder configuration with a clear reference beam and standard QPI reconstruction based on Fourier filtering) as ground-truth method. Fig. 4 includes the results for the case of FOV_2. Fig. 4(a) and (c) include the QPIs recovered from the proposed CIM and conventional DHM, respectively, where we also include enlarged (and rotated) images of the ROIs enclosed in blue and green rectangles, respectively. From QPIs, we computed the 3D thickness distributions $t(x,y)$ according to the relation

$$t(x,y) = \frac{\varphi(x,y)\lambda}{2\pi\Delta n} \tag{10}$$

being λ the illumination wavelength, $\Delta n = n_{test} - n_{air}$ the RI difference between the test structures and the air, and $\varphi(x,y)$ the phase distribution of those structures. Fig. 4(b) and (d) include the rotated 3D thickness distributions computed from Eq. (10) and within the blue and green ROIs, respectively. From Fig. 4(a)–(d), we can realize that both CIM and DHM methods provided equivalent results. Finally, we performed phase and thickness profiles along the red and black dashed lines included in enlarged images of Fig. 3(a) and (c), respectively. The results are included in Fig. 4(e), exhibiting a good agreement between the profiles provided by both methods. In Table 1, the average thickness values of such structures computed from Fig. 4(e) are compared with the nominal value and the value estimated by atomic force microscopy (AFM) both provided by the manufacturer. The errors in the thickness values are provided by computing the standard deviation (SD) of the maximum and minimum thickness values achieved from the different periods of the grating. The agreement between values demonstrates that automated CIM approach provides accurate QPI and thickness values when considering a 20x/0.42NA microscope lens.

Additional validation of the proposed automated CIM approach is

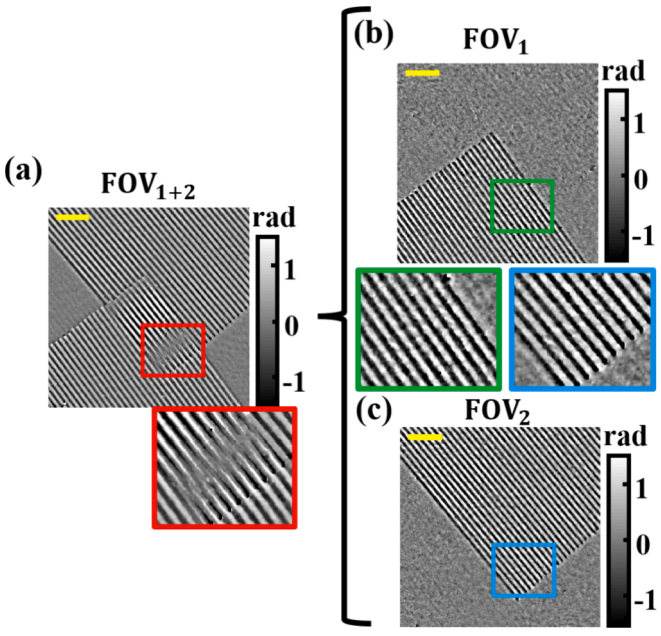

Fig. 3. Experimental results of the SSC decoupling process of the proposed automated CIM approach involving a grid square of the QPT™ and a 20x/0.42NA microscope lens. (a) QPI reconstruction after Fourier filtering including both coupled FOV_1 and FOV_2 where enlarged ROI within red rectangle shows the phase cancellation. (b) and (c) QPIs of FOV_1 and FOV_2, respectively, after SSC implementation exhibiting proper decoupling, where enlarged images of green and blue ROIs show successful removal of phase cancelation and proper QPI reconstruction. Scale bars are 20 μm. (For interpretation of the references to color in this figure legend, the reader is referred to the web version of this article.)

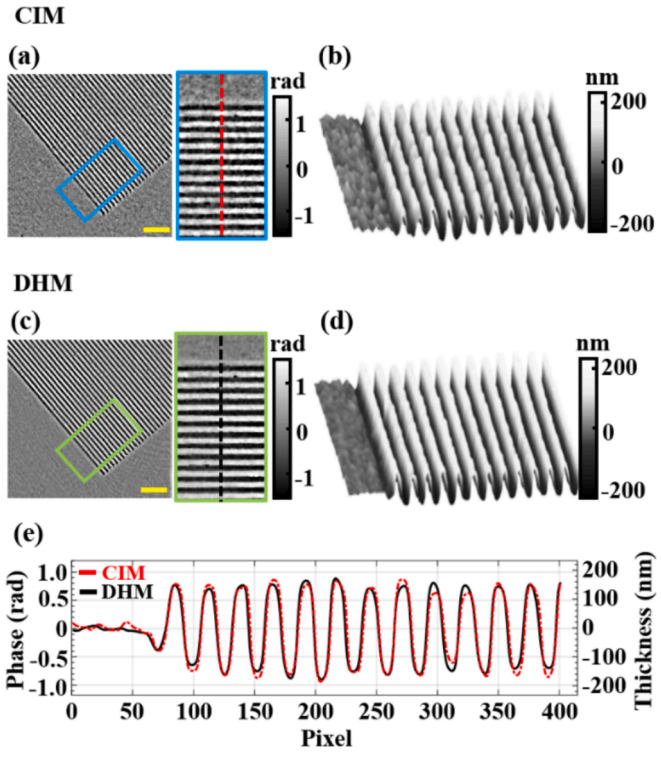

Fig. 4. Quantitative comparison of experimental results provided by the proposed automated CIM approach against standard off-axis DHM for the case of a square grid structure imaged with a 20x/0.42NA microscope lens. (a) and (c) Retrieved QPIs and (b) and (d) thickness distributions provided by CIM and DHM, respectively. (e) Quantitative phase-thickness profiles along red and black dashed lines marked in enlarged images of (a) and (c), respectively. Scale bars are 20 μm. (For interpretation of the references to color in this figure legend, the reader is referred to the web version of this article.)

Table 1
Quantitative analysis of the new automated CIM approach with 20x/0.42NA microscope lens involving a quantitative phase target. Comparison of thickness values provided by automated CIM, conventional off-axis DHM and the manufacturer (nominal and estimated by AFM) for the phase structures of FOV_2.

	Thickness ± SD (nm)
Nominal	300
Estimated by AFM	329.5
Measured by automated CIM	314 ± 30
Measured by conventional DHM	306 ± 24

Table 2
Quantitative analysis of the new automated CIM approach with 50x/0.55NA microscope lens involving a quantitative phase target. Comparison of thickness values provided by automated CIM, conventional off-axis DHM and the manufacturer (nominal and estimated by AFM) for the phase structures of FOV_2.

	Thickness ± SD (nm)
Nominal	200
Estimated by AFM	223.4
Measured by automated CIM	236 ± 15
Measured by conventional DHM	227 ± 9

reported using a 50x/0.55NA microscope lens. In this case, a square grid of the same QPT™ with a nominal thickness of 200 nm was involved. The results are included through Fig. 5. Fig. 5(a) shows the QPI recovered after Fourier filtering of one of the three recorded holograms required for SSC application, including an enlarged ROI to better identify phase cancellation effect. After SSC decoupling algorithm, we achieved the QPIs included in Fig. 5(b) and (c) for FOV_1 and FOV_2, respectively. As we can see in the enlarged images of the RIOs enclosed within the green and blue regions in Fig. 5(b) and (c), respectively, the SSC algorithm successfully decoupled both FOVs each other, even in the ROIs with phase cancellation, thus making the grid structures visible.

Furthermore, the accuracy for QPI reconstruction was validated, as before, through the comparison of the QPI values of the FOV_2 with the provided by conventional DHM as ground-truth technique. In particular, we compared the QPI distributions provided by both techniques in the ROI within the white rectangle marked in Fig. 5(c). The recovered QPIs are included in Fig. 5(d) and (e) for the case of CIM and DHM, respectively, whereas the 3D thickness distributions, computed from Eq. (10) and the QPI values, are shown in Fig. 5(f) and (g), respectively. As we can see, although the QPIs and thickness distributions recovered from CIM appeared noisier than the provided by standard DHM, both techniques provided similar distributions. Finally, we computed the quantitative phase-thickness profiles along the dashed red and black lines included in Fig. 5(d) and (e), whose results are included in Fig. 5(h). Looking at Fig. 5(h), we can realize that both techniques provided comparable phase-thickness values each other. As before, we compare the average thickness values computed from Fig. 5(h) with the provided by the manufacturer, and the results are shown in Table 2. Again, the results of Table 2 exhibit a high concordance one another, validating the new CIM approach for accurate QPI employing the 50x/0.55NA microscope lens. Hence, with these two experimental validations, we demonstrated the feasibility of CIM to be successfully performed with microscope lenses having medium magnifications and NAs.

3.2. Experimental validation with biological samples

The automated CIM approach was also evaluated for imaging of biological samples. To demonstrate that the approach reported here can also provide QPI in diverse biological scenarios, it was validated with diverse type of samples (prostate cancer cells, red blood cells, and mouse fatty live tissues) with the previous microscope lenses (20x/0.42NA and 50x/0.55NA).

In a first experiment involving biological samples, we imaged two different cell lines (PC-3 and LNCaP) of fixed prostate cancer cells using the 20x/0.42NA microscope lens. Prostate cancer cells were prepared as follows. Cells were first cultured in RPMI 1640 medium with 10 % fetal bovine sertum, 100 U/ml Penincillin and 0.1 μg/ml Streptomycine at standard cell culture conditions (37 °C in 5 % CO_2 in a humidified incubator). After cell confluent stage was reached, cells were released from the culture support and centrifuged. Finally, supernatant fluid was discarded by centrifugation and cells were resuspended in a cytopreservative solution and mounted in a microscope slide for imaging.

Fig. 6 presents an example of the experimental results provided by the proposed CIM approach for the case of PC-3 (left half – number 1 of Fig. 6) and LNCaP (right half – number 2 of Fig. 6) prostate cancer cells. Looking through Fig. 6, we can observe that PC-3 cells were mostly presented as individual cells, whereas LNCaP cells tended to aggregate each other and to conform clusters. Hence, two different cellular cases

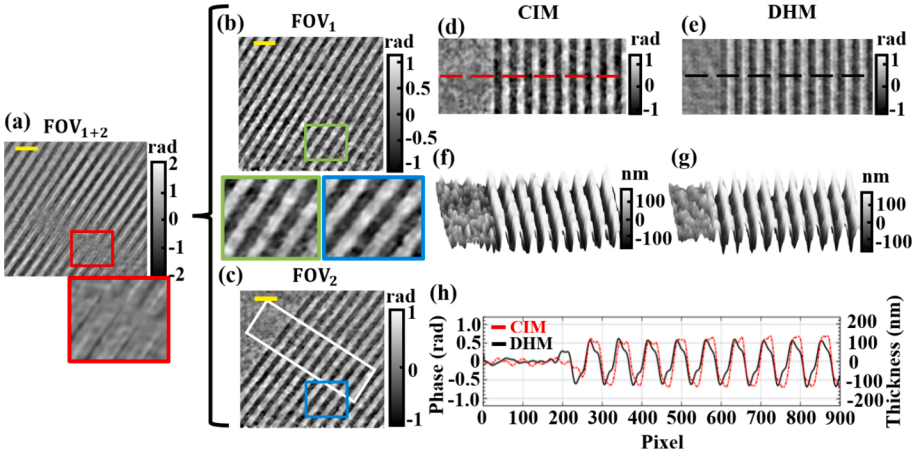

Fig. 5. Experimental validation of the proposed automated CIM approach with a 50x/0.55NA microscope lens and involving a grid square of the QPT™. (a) QPI reconstruction after Fourier filtering including both coupled FOV_1 and FOV_2 where enlarged ROI within red rectangle shows the phase cancellation. (b) and (c) QPIs of FOV_1 and FOV_2, respectively, after SSC implementation exhibiting proper decoupling, where enlarged images of green and blue ROIs show successful removal of phase cancelation and proper QPI reconstruction. (d) and (e) QPIs retrieved from CIM and DHM, respectively, of the ROI marked with white rectangle in (c). (f) and (g) 3D thickness distributions computed considering Eq. (10) and QPIs included in (d) and (e) for the case of CIM and DHM, respectively. (h) Quantitative phase-thickness profiles along red and black dashed lines marked in enlarged images in (d) and (e), respectively. Scale bars are 10 μm. (For interpretation of the references to color in this figure legend, the reader is referred to the web version of this article.)

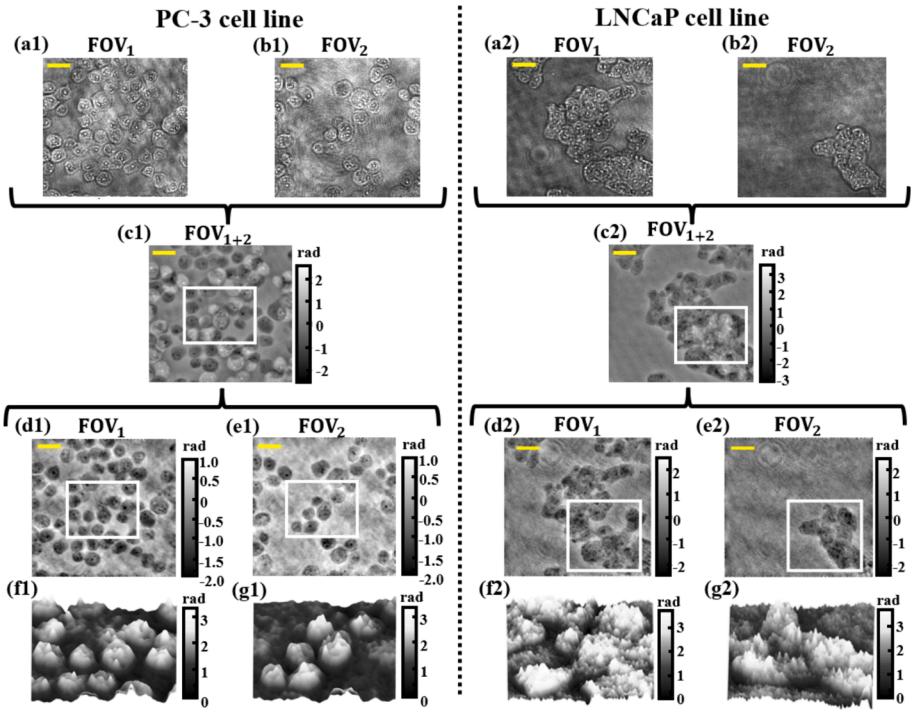

Fig. 6. Experimental results provided by automated CIM system involving PC-3 (1) and LNCaP (2) prostate cancer cell lines imaged with a 20x/0.42NA microscope lens. (a) and (b) Intensity images of FOV_1 and FOV_2 recorded from each interferometric beam, respectively. (c) Reconstructed QPI of the coupled FOVs after Fourier filtering implementation. (d) and (e) Reconstructed QPIs of the decoupled FOV_1 and FOV_2 after SSC application, respectively. (f) and (g) Enlarged perspective QPI views of cells included in white rectangles of (d) and (e), respectively. Scale bars are 20 μm.

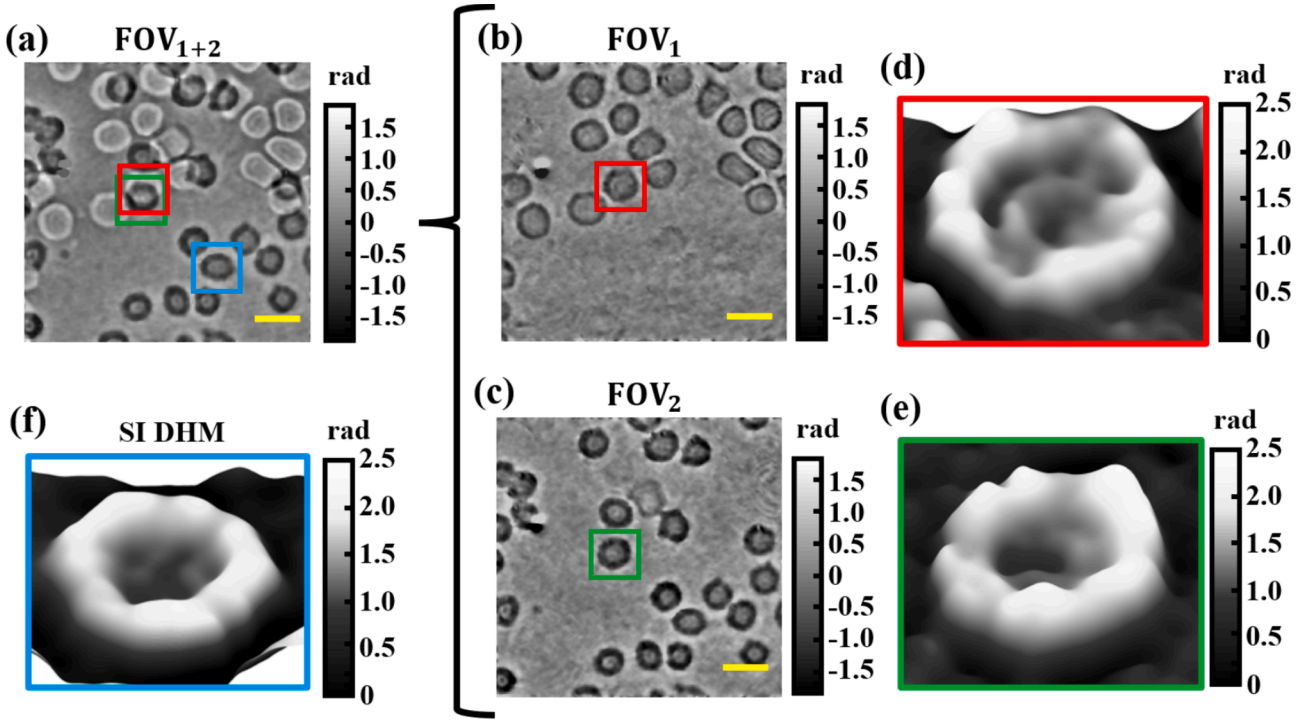

Fig. 7. Experimental results provided by the proposed CIM approach involving RBCs imaged with a 50x/0.55NA microscope lens. (a) QPI reconstruction of the coupled FOVs after Fourier filtering. (b) and (c) QPI reconstructions of the FOV_1 and FOV_2 decoupled by SSC application, respectively. (d) and (e) Enlarged perspective QPI views of cells included in red and green squares of (b) and (c), respectively. (f) Enlarged perspective QPI view of the cell included in the blue square of (a) for comparison with the results provided by ground-truth SI DHM. Scale bars are 10 μm. (For interpretation of the references to color in this figure legend, the reader is referred to the web version of this article.)

were studied in this case. Fig. 6(a) and (b) include the intensity images recorded from each individual beam (named as FOV_1 and FOV_2, respectively) to show that both interferometric branches contained sample information. In addition, we present in Fig. 6(c) one of the three QPI reconstructions achieved after Fourier filtering, showing the overlapping between both FOVs. Furthermore, QPI reconstructions of FOV_1 and FOV_2 after application of SSC method are depicted in Fig. 6(d) and (e), respectively. Moreover, to clearly show the successful decoupling of both FOVs, we include in Fig. 6(f) and (g) enlarged perspective views of QPI reconstructions of the cells within the regions marked with white rectangles in Fig. 6(d) and (e), respectively. Comparing Fig. 6(d) and (e) with Fig. 6(a) and (b), respectively, we can see that the proposed CIM method provided successful separation of the FOVs coming from the different interferometric beams. In addition, QPI reconstructions presented through Fig. 6(d)–(g) demonstrate that the proposed approach provided satisfactory QPI reconstructions of biological samples containing individual cells as well as cell cluster aggregations.

In a second experiment, a sample of red blood cells (RBCs) was imaged using the 50x/0.55NA microscope lens. RBCs, freely donated by a cell biology laboratory, were obtained from a puncture drop on the finger skin and smeared onto a microscope slide for imaging. An example of the experimental results is included in Fig. 7. Fig. 7(a) shows one of the QPI reconstructions achieved after Fourier filtering implementation including both coupled FOVs. In addition, Fig. 7(b) and (c) present QPI reconstructions, in positive phase contrast, of the decoupled FOV_1 and FOV_2 after application of SSC method, exhibiting successful separation between both FOVs. To emphasize successful decoupling of overlapping individual cells, we include in Fig. 7(d) and (e) magnified perspective views of the QPI reconstructions for the RBCs within the red and green squares included in Fig. 7(b) and (c), respectively. For visual comparison, Fig. 7(f) includes a perspective view of the QPI reconstruction for a non-overlapped RBC, marked with blue square in Fig. 7 (a), which can be considered as a QPI provided by standard self-interference (SI) DHM, considered in this case as the ground-truth method. Although QPIs included in Fig. 7(d)–(f) correspond to different RBCs, we can notice a high concordance between the results provided by the proposed CIM approach and the results provided by the ground-truth SI DHM technique.

And finally, we evaluated the presented approach for QPI of a biological sample consisting of a mouse fatty liver histology. The sample was prepared as follows. First, liver was processed by fixation with 4 % PFA for 4 h, followed by tissue dehydration and paraffin embedding.

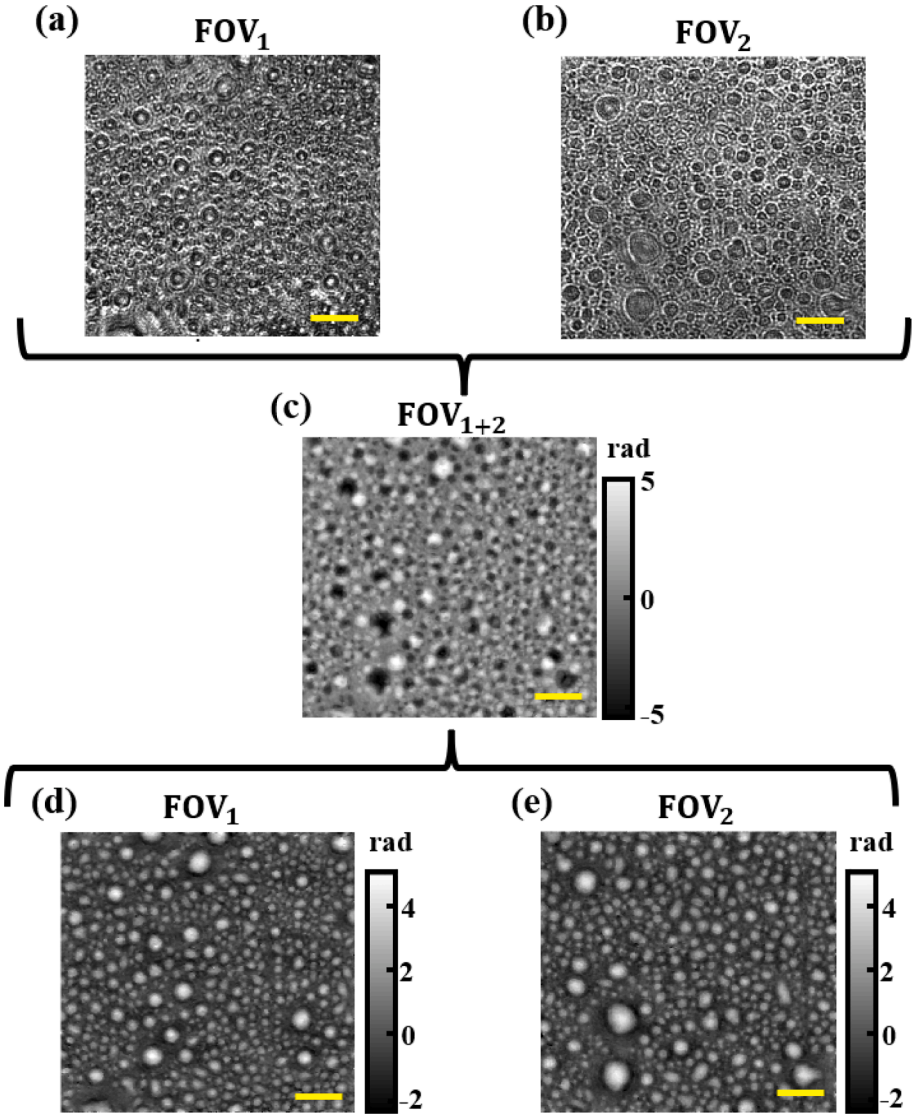

Fig. 8. Experimental results provided by the automated CIM approach with a 20x/0.42NA microscope lens for the case of a mouse fatty liver tissue with 100 % confluency. (a) and (b) Intensity images of FOV_1 and FOV_2 recorded from each individual beam, respectively. (c) Reconstructed QPI of the coupled FOVs after Fourier filtering implementation. (d) and (e) Reconstructed QPIs of the decoupled FOV_1 and FOV_2 after SSC application, respectively. Scale bars are 20 μm.

Then, liver tissue was cut with a microtome to obtain slides with sections of 5 μm. Finally, slides with liver sections were deparaffinised and hydrated before mounting with coverslips and mounting media for imaging. This sample was different to the samples previously studied and was considered as challenging due to its high confluency. Briefly, confluency can be defined as the percentage area covered by cells in a culture dish or flask [30]. According to this definition, the sample here analysed had a confluency of 100 %.

Fig. 8 shows an example of the experimental results achieved for that liver sample utilizing the 20x/0.42NA microscope lens. For easy identification of the two FOVs to be reconstructed, Fig. 8(a) and (b) include the intensity images recorded for each individual FOV_1 and FOV_2, respectively, before setting the interferometric configuration. Furthermore, Fig. 8(c) shows one of the three QPI images recovered after Fourier filtering procedure, where the lipid droplets of the fatty liver tissue contained in the different FOVs can be identified due to their opposite phase contrast. Moreover, decoupled QPI images of FOV_1 and FOV_2 after SSC reconstruction are shown in Fig. 8(c) and (d). In this case, comparison against results provided by a standard common-path DHM approach was not possible due to the high confluence nature of the tissue sample. Nevertheless, visual comparison between the intensity images of Fig. 8(a) and (b) and QPIs of Fig. 8(d) and (e) suggests that both FOVs were successfully decoupled and reconstructed.

4. Discussion

In this contribution, we have extended the use of our recently proposed CIM concept to medium NA microscope lenses. In particular, we have presented and experimentally validated a new automated CIM layout based on a quasi-common-path Mach-Zehnder interferometer. The method achieves QPI of two FOVs by sequentially recording three off-axis holograms, incorporating a 1-pixel shift (both horizontally and vertically) in one of the interferometric beams between consecutive holograms. Through Fourier filtering and SSC procedures applied to these holograms, the decoupling and QPI of both beams was successfully accomplished. Experimental validations with calibrated phase objects demonstrated the approach's effectiveness in separating information from both complex beams, thereby doubling the achievable FOV compared to conventional DHM. The proposed method also provided accurate QPI and 3D thickness distributions, even in challenging scenarios with phase cancellation. Evaluations with diverse types of fixed cells and tissue sections demonstrated the suitability of the approach for biological imaging, even in cases of high sample confluency.

In CIM technique, a critical consideration is how to generate lateral shifts (both horizontal and vertical) required for SSC implementation in one of the FOVs. On the previous implementation with a Michelson arrangement [27], such shifts were achieved through using precise displacements performed with a motorized linear translation stage (1-pixel shift between consecutive holograms) while manual interaction by the user was needed to change the off-axis direction in one of the mirrors in the Michelson configuration. This manual mirror manipulation presents several drawbacks. On one hand, it reduces considerably the acquisition time of the full sequence of recorded images (around 1 min) since the off-axis angle needs to be properly adjusted for the second direction (recording of one hologram, inspection of its Fourier transform and readjusting the off-axis angle repeating the procedure). On the other hand, the manual control of the mirror arrangement prevented repeatability in the recording conditions, which is a critical issue for spreading CIM to real application scenarios. On the contrary, in this contribution, the recording process is fully automatized, ensuring both reduced acquisition times (only a few seconds for whole recording process) and high repeatability, therefore approaching CIM to the conditions encountered in real technical and biomedical applications.

As in previous CIM approach [27], holograms were recorded considering FOV shifts along vertical and horizontal directions but alternative pair of orthogonal (or even non-orthogonal) directions could also be considered. This is because the shift in the second direction is only required to reduce the indeterminate line in the complex Cepstrum to the DC term, making it analogous to the zero-ambiguity problem encountered in transport of intensity equation (TIE) QPI methodologies [13]. Nevertheless, various strategies, including high-pass filtering (utilized here for simplicity), Zernike functions, polynomial fitting, principal component analysis, and machine learning, can be employed to address this issue [31–35].

Similar to DHM, CIM is a versatile technique adaptable to different interferometric layouts (Michelson, Mach-Zender, common-path, etc.) and holographic configurations (not only off-axis but also slightly off-axis or on-axis configurations). In terms of temporal resolution, automated CIM implementation requires three off-axis holograms, one hologram less than previous CIM methodology [27] and comparable again to the holograms needed for phase-shifting (PS) methods in DHM. In addition, the optomechanical components required for CIM to induce the shift between FOVs are also similar to the equipment needed in PS-based DHM techniques to provide the phase shift between interferometric beams. However, CIM stands out favourably compared to PS methods by increasing the FOV (doubling or tripling depending on CIM implementation) and eliminating reference beam constraints. On the other hand, CIM under off-axis holographic configuration limits the pixel size of the digital sensor due to the wider circular mask defined in the Fourier filtering process compared to classical off-axis DHM. In CIM, the cross-correlation term contains information about two complex fields with spatial distribution, doubling the cut-off spatial frequency for this term, unlike classical DHM approaches where clear reference beams have a planar spatial distribution (delta function at the Fourier domain). However, modern QPI methodologies based on Hilbert-Huang transform [36,37] or Kramers-Kronig relations [38,39] can be applied to optimize spatial bandwidth usage.

In comparison to common-path DHM techniques, CIM enhances flexibility in the recording interferometric process by avoiding sample constraints (sparse, confined, etc.) typically imposed in common-path DHM approaches. Standard common-path DHM techniques, such as spatially-multiplexed [40–42] or self-interference [43–45] approaches, require clean reference beams obtained directly from the transmission of light through sample regions without object information. These constraints are critical when applied to biological studies where samples are often large and exhibit high confluency, as seen in histology, involving tissue studies with lengths of millimetres and confluences up to 100 %. In contrast, the CIM technique is well-suited for such biological applications not only because it avoids the need for clear regions in the sample but also because it increases the analysed FOV. Moreover, no bulky/complex setups are required to generate a clear reference beam. Consequently, the proposed automated methodology stands as a promising candidate for integration into existing commercial bright-field microscopes, facilitating the enhancement of coherence sensing capabilities with minimal modifications. This aligns with the current trend of democratizing science, enabling QPI in biological experiments for laboratories with constrained budgets.

5. Conclusions

In summary, this contribution reported on a step forward in the development of the CIM methodology, specifically for its application in real biological scenarios with pseudo real-time capabilities where the manual user's interaction for the interferometric conditions (required in previous approach [27]) is no longer needed. Additional differences with previous implementation [27] come from the use of a quasi-common-path Mach-Zehnder interferometric configuration (instead of a Michelson layout), the usage of medium NA microscope lenses (20x/0.42NA and 50x/0.55NA) instead of low NA ones, and the recording of 3 off-axis holograms (instead of 4). As consequence, the FOV is doubled in comparison with the tripled one reported in Ref. [27] but the use of medium NA objectives, process automatization and measurement

repeatability are desirable requirements in most applications in cell biology. Notice that the fact that this new CIM implementation has been validated with medium NA microscope objectives does not prevent its use with low NA lenses as in previous work [27] meaning that both manuscripts are complementary and not exclusive one each other, presenting implementations of a novel QPI method under different experimental conditions.

As any ground-breaking interferometry-based QPI methodology, CIM challenges the conventional requirement in most interferometry fields for a clear reference beam with no sample information. CIM achieves the information from decoupling the different complex fields involved in the interferometric process, providing accurate QPI and FOV doubling in the automated implementation here presented or even tripling its value [27]. In consequence, CIM imposes no restrictions or prior knowledge about the interferometric beams, eliminating the need of a clear (or with known complex distribution) reference beam, a common requirement in conventional DHM approaches. Next steps of the technique include fast imaging (video rate), noise reduction and implementation in real microscope setups.

Funding

This research has been funded by the Grant PID2020-120056 GB-C21 funded by MCIN/AEI/https://doi.org/10.13039/501100011033. J. A. Picazo-Bueno is supported by the Spanish grant "Margarita Salas" (Ref. MS21-100), proposed by the Ministry of Universities of the Government of Spain (UP2021-044) funded by the European Union, NextGenerationEU.

CRediT authorship contribution statement

Ricardo Rubio-Oliver: Writing – review & editing, Validation, Software, Methodology, Formal analysis. **Vicente Micó:** Writing – review & editing, Visualization, Validation, Supervision, Resources, Project administration, Methodology, Funding acquisition. **Zeev Zalevsky:** Writing – review & editing, Validation, Conceptualization. **Javier García:** Writing – review & editing, Validation, Supervision, Formal analysis, Data curation, Conceptualization. **Jose Angel Picazo-Bueno:** Writing – original draft, Validation, Supervision, Software, Investigation, Data curation.

Declaration of competing interest

The authors declare that they have no known competing financial interests or personal relationships that could have appeared to influence the work reported in this paper.

Data availability

Data will be made available on request.

Acknowledgments

Authors thank to Dr. Andrea Herrero-Cervera, from Health Research Institute Clinic Hospital of Valencia – INCLIVA (Spain) for providing us the sample of mouse fatty liver histology.

References

[1] Y.K. Park, C. Depeursinge, G. Popescu, Quantitative phase imaging in biomedicine, Nat Photonics 12 (2018) 578–589.
[2] N.T. Shaked, S.A. Boppart, L.V. Wang, J. Popp, Label-free biomedical optical imaging, Nat Photonics 17 (2023) 1031–1041, https://doi.org/10.1038/s41566-023-01299-6.
[3] G. Popescu, Quantitative phase imaging of cells and tissues, McGraw-Hill, 2011.
[4] B. Kemper, A. Bauwens, D. Bettenworth, M. Götte, B. Greve, L. Kastl, et al., Label-Free Quantitative in Vitro Live Cell Imaging with Digital Holographic Microscopy, vol. 2, Springer, Cham, 2019, 10.1007/11663_2019_6.
[5] T.L. Nguyen, S. Pradeep, R.L. Judson-Torres, J. Reed, M.A. Teitell, T.A. Zangle, Quantitative phase imaging: recent advances and expanding potential in biomedicine, ACS Nano 16 (2022) 11516–11544, https://doi.org/10.1021/ACSNANO.1C11507/ASSET/IMAGES/LARGE/NN1C11507_0009.JPEG.
[6] M.R. Teague, Deterministic phase retrieval: a Green's function solution, J Opt Soc Am 73 (1983) 1434–1441, https://doi.org/10.1364/JOSA.73.001434.
[7] N. Streibl, Phase imaging by the transport equation of intensity, Opt Commun 49 (1984) 6–10, https://doi.org/10.1016/0030-4018(84)90079-8.
[8] D. Paganin, K.A. Nugent, Noninterferometric phase imaging with partially coherent light, Phys Rev Lett 80 (1998) 2586–2589, https://doi.org/10.1103/PhysRevLett.80.2586.
[9] B.C. Platt, R. Shack, History and principles of Shack-Hartmann wavefront sensing, J Refract Surg 17 (2001) 573, https://doi.org/10.3928/1081-597x-20010901-13.
[10] L. Waller, L. Tian, Quantitative differential phase contrast imaging in an LED array microscope, Opt Express 23 (2015) 11394–11403, https://doi.org/10.1364/OE.23.011394.
[11] P. Marquet, B. Rappaz, P.J. Magistretti, E. Cuche, Y. Emery, T. Colomb, et al., Digital holographic microscopy: a noninvasive contrast imaging technique allowing quantitative visualization of living cells with subwavelength axial accuracy, Opt Lett 30 (2005) 468–470, https://doi.org/10.1364/ol.30.000468.
[12] B. Bhaduri, C. Edwards, H. Pham, R. Zhou, T.H. Nguyen, L.L. Goddard, et al., Diffraction phase microscopy: principles and applications in materials and life sciences, Adv Opt Photonics 6 (2014) 57–119, https://doi.org/10.1364/aop.6.000057.
[13] C. Zuo, J. Li, J. Sun, Y. Fan, J. Zhang, L. Lu, et al., Transport of intensity equation: a tutorial, Opt Lasers Eng 135 (2020) 106187, https://doi.org/10.1016/j.optlaseng.2020.106187.
[14] B. Kemper, G. von Bally, Digital holographic microscopy for live cell applications and technical inspection, Appl Opt 47 (2008) A52–A61, https://doi.org/10.1364/AO.47.000A52.
[15] M.K. Kim, Digital holographic microscopy. Principles, Techniques, and Applications, Springer, US, 2011.
[16] T. Cacace, V. Bianco, P. Ferraro, Quantitative phase imaging trends in biomedical applications, Opt Lasers Eng 135 (2020) 106188, https://doi.org/10.1016/J.OPTLASENG.2020.106188.
[17] J. Kühn, F. Charrière, T. Colomb, E. Cuche, F. Montfort, Y. Emery, et al., Axial sub-nanometer accuracy in digital holographic microscopy, Meas Sci Technol (2008; 19.), https://doi.org/10.1088/0957-0233/19/7/074007.
[18] P. Langehanenberg, B. Kemper, D. Dirksen, G. Von Bally, Autofocusing in digital holographic phase contrast microscopy on pure phase objects for live cell imaging, Appl Opt (2008;47.), https://doi.org/10.1364/AO.47.00D176.
[19] N.T. Shaked, V. Micó, M. Trusiak, A. Kuś, S.K. Mirsky, Off-axis digital holographic multiplexing for rapid wavefront acquisition and processing, Adv Opt Photonics 12 (2020) 611, https://doi.org/10.1364/aop.384612.
[20] T. Zhang, I. Yamaguchi, Three-dimensional microscopy with phase-shifting, Opt Lett 23 (1998) 1221–1223, https://doi.org/10.1364/ol.23.001221.
[21] F. Dubois, L. Joannes, J.-C. Legros, Improved three-dimensional imaging with a digital holography microscope with a source of partial spatial coherence, Appl Opt 38 (1999) 7085, https://doi.org/10.1364/ao.38.007085.
[22] H. Iwai, C. Fang-Yen, G. Popescu, A. Wax, K. Badizadegan, R.R. Dasari, et al., Quantitative phase imaging using actively stabilized phase-shifting low-coherence interferometry, Opt Lett 29 (2004) 2399, https://doi.org/10.1364/ol.29.002399.
[23] D.M. Gale, M.I. Pether, J.C. Dainty, Linnik microscope imaging of integrated circuit structures, Appl Opt 35 (1996) 131, https://doi.org/10.1364/ao.35.000131.
[24] G.S. Kino, S.S.C. Chim, Mirau correlation microscope, Appl Opt 29 (1990) 3775, https://doi.org/10.1364/ao.29.003775.
[25] S. Reichelt, H. Zappe, Combined Twyman-Green and Mach-Zehnder interferometer for microlens testing, Appl Opt 44 (2005) 5786–5792, https://doi.org/10.1364/AO.44.005786.
[26] G. Popescu, T. Ikeda, R.R. Dasari, M.S. Feld, Diffraction phase microscopy for quantifying cell structure and dynamics, Opt Lett 31 (2006) 775, https://doi.org/10.1364/ol.31.000775.
[27] R. Rubio-Oliver, J. García, Z. Zalevsky, J.Á. Picazo-Bueno, V. Micó, Cepstrum-based interferometric microscopy (CIM) for quantitative phase imaging, Opt Laser Technol 174 (2024) 110626, https://doi.org/10.1016/J.OPTLASTEC.2024.110626.
[28] E. Cuche, P. Marquet, C. Depeursinge, Spatial filtering for zero-order and twin-image elimination in digital off-axis holography, Appl Opt 39 (2000) 4070, https://doi.org/10.1364/ao.39.004070.
[29] T.J. Flynn, Two-dimensional phase unwrapping with minimum weighted discontinuity, J Opt Soc Am A 14 (1997) 2692–2701, https://doi.org/10.1364/JOSAA.14.002692.
[30] C.H. Chiu, L.J. Der, T.T. Lin, P.H. Su, W.C. Li, Y.J. Lee, et al., Systematic Quantification of Cell Confluence in Human Normal Oral Fibroblasts, Appl Sci 10 (2020) 9146, https://doi.org/10.3390/APP10249146.
[31] L. Miccio, D. Alfieri, S. Grilli, P. Ferraro, A. Finizio, L. De Petrocellis, et al., Direct full compensation of the aberrations in quantitative phase microscopy of thin objects by a single digital hologram, Appl Phys Lett 90 (2007) 041104, https://doi.org/10.1063/1.2432287/333625.
[32] Kim MK. Principles and techniques of digital holographic microscopy. SPIE Rev 2010;1. Doi: 10.1117/6.0000006.
[33] C. Zuo, W. Qu, Q. Chen, A. Asundi, Phase aberration compensation in digital holographic microscopy based on principal component analysis, Opt Lett 38 (2013) 1724–1726, https://doi.org/10.1364/OL.38.001724.

[34] S. Liu, Q. Lian, Z. Xu, Phase aberration compensation for digital holographic microscopy based on double fitting and background segmentation, Opt Lasers Eng 115 (2019) 238–242, https://doi.org/10.1016/J.OPTLASENG.2018.12.001.
[35] T. Nguyen, V. Bui, V. Lam, C.B. Raub, L.-C. Chang, G. Nehmetallah, Automatic phase aberration compensation for digital holographic microscopy based on deep learning background detection, Opt Express 25 (2017) 15043–15057, https://doi.org/10.1364/OE.25.015043.
[36] J.Á. Picazo-Bueno, M. Trusiak, J. García, K. Patorski, V. Micó, Hilbert-Huang single-shot spatially multiplexed interferometric microscopy, Opt Lett 43 (2018) 1007, https://doi.org/10.1364/ol.43.001007.
[37] M. Trusiak, M. Cywinska, V. Mico, J.A. Picazo-Bueno, C. Zuo, P. Zdankowski, et al., Variational Hilbert Quantitative Phase Imaging, Sci Reports 2020 (101) (2020.1–16.) 10, https://doi.org/10.1038/s41598-020-69717-1.
[38] Y. Baek, K. Lee, S. Shin, Y. Park, Kramers-Kronig holographic imaging for high-space-bandwidth product, Optica 6 (2019) 45–51, https://doi.org/10.1364/OPTICA.6.000045.
[39] Y. Baek, Y. Park, Intensity-based holographic imaging via space-domain Kramers-Kronig relations, Nat Photonics 15 (2021) 354–360, https://doi.org/10.1038/s41566-021-00760-8.
[40] V. Mico, C. Ferreira, Z. Zalevsky, J. García, Spatially-multiplexed interferometric microscopy (SMIM): converting a standard microscope into a holographic one, Opt Express 22 (2014) 14929, https://doi.org/10.1364/oe.22.014929.
[41] S. Ebrahimi, M. Dashtdar, E. Sánchez-Ortiga, M. Martínez-Corral, B. Javidi, Stable and simple quantitative phase-contrast imaging by Fresnel biprism, Appl Phys Lett 112 (2018) 1–5, https://doi.org/10.1063/1.5021008.
[42] M. Trusiak, J.-A. Picazo-Bueno, K. Patorski, P. Zdańkowski, V. Mico, Single-shot two-frame π-shifted spatially multiplexed interference phase microscopy, J Biomed Opt 24 (2019) 096004, https://doi.org/10.1117/1.jbo.24.9.096004.
[43] B. Kemper, A. Vollmer, G. von Bally, C.E. Rommel, J. Schnekenburger, Simplified approach for quantitative digital holographic phase contrast imaging of living cells, J Biomed Opt 16 (2011) 026014, https://doi.org/10.1117/1.3540674.
[44] A.S.G. Singh, A. Anand, R.A. Leitgeb, B. Javidi, Lateral shearing digital holographic imaging of small biological specimens, Opt Express 20 (2012) 23617, https://doi.org/10.1364/oe.20.023617.
[45] A. Anand, V. Chhaniwal, B. Javidi, Tutorial: Common path self-referencing digital holographic microscopy, APL Photonics 3 (2018) 071101, https://doi.org/10.1063/1.5027081.